Tectonophysics 493 (2010) 272–284

Contents lists available at ScienceDirect

Tectonophysics

journal homepage: www.elsevier.com/locate/tecto

Supershear transition due to a free surface in 3-D simulations of spontaneous dynamic rupture on vertical strike-slip faults

Y. Kaneko [a,*], N. Lapusta [b]

[a] Division of Geological and Planetary Sciences, California Institute of Technology, 1200 E. California Boulevard MC 252-21, Pasadena, CA 91125, USA
[b] Division of Geological and Planetary Sciences and Division of Engineering and Applied Science, California Institute of Technology, 1200 E. California Blvd. MC104-44, Pasadena, CA 91125, USA

ARTICLE INFO

Article history:
Received 12 November 2009
Received in revised form 1 June 2010
Accepted 21 June 2010
Available online 1 July 2010

Keywords:
Supershear transition
Earthquake rupture dynamics
Earthquake source physics

ABSTRACT

Supershear rupture propagation has been inferred from seismic observations for natural faults and observed in laboratory experiments. We study the effect of the free surface on the transition of earthquake rupture from subshear to supershear speeds using simulations of spontaneous dynamic rupture on vertical strike-slip faults. We find that locally supershear rupture near the free surface can occur due to (i) the generalized Burridge–Andrews mechanism, that is, a supershear loading field between *P*- and *SV*-wave arrivals generated by the main rupture front at depths, and (ii) the phase conversion of *SV* to *P*-diffracted waves at the free surface. Weaker supershear slip due to the generalized Burridge–Andrews mechanism is caused by the low strength at shallow portions of the fault relative to deeper ones. Dominant supershear rupture is supported by the additional supershear loading field produced by phase conversion. Locally supershear propagation at the free surface occurs regardless of the level of prestress and can cause transition to supershear propagation over the entire seismogenic depth. Such global supershear transition, which depends on prestress, can occur under prestress levels lower than the theoretical estimates for models with no free surface. Although the effectiveness of supershear transition due to the free surface can be diminished by several potentially important factors, it may play an important role on natural faults, at least in those strike-slip earthquakes that accumulate significant surface slip.

1. Introduction

Recent improvements in availability and quality of strong-motion data revealed variability of rupture speeds in large crustal earthquakes. Seismological inversions show that average rupture speeds of many earthquakes are about 80% of the *S* wave speed of the surrounding medium (Heaton, 1990), i.e. earthquakes have subshear rupture speeds on average. However, supershear rupture speeds that exceed the *S* wave speed of the medium have been inferred for several large strike-slip earthquakes, including the 1979 Imperial Valley earthquake (Archuleta, 1984; Spudich and Cranswick, 1984), the 1999 Kocaeli (Izmit) earthquake (Bouchon et al., 2000, 2001), the 1999 Duzce earthquake (Bouchon et al., 2001; Konca et al., 2010), the 2001 Kokoxili (Kunlun) earthquake (Bouchon and Vallée, 2003; Robinson et al., 2006; Vallée et al., 2008; Walker and Shearer, 2009), and the 2002 Denali earthquake (Dunham and Archuleta, 2004; Ellsworth et al., 2004). The possibility of the occurrence of such phenomena has been confirmed in laboratory studies (Rosakis et al., 1999; Xia et al., 2004; Lu et al., 2007, 2009).

Variability of earthquake rupture speeds, either subshear or supershear, has important implications for seismic radiation and the resulting ground motion. In the case of supershear ruptures, radiating *S* waves can constructively form a Mach front that transports large seismic stress and particle velocity far from the fault (Bernard and Baumont, 2005; Dunham and Archuleta, 2005; Bhat et al., 2007; Dunham and Bhat, 2008). The directivity pattern of supershear rupture can also be different from that of subshear rupture (Aagaard and Heaton, 2004). Bouchon and Karabulut (2008) showed that earthquakes with inferred supershear speeds have a characteristic pattern of aftershocks, with almost no aftershocks on the fault plane and clusters of them on secondary structures off the fault plane. Hence it is important to understand the conditions controlling the transition of earthquake ruptures from sub-Rayleigh to supershear speeds during destructive large earthquakes.

The problem of sub-Rayleigh-to-supershear transition has been theoretically analyzed in a number of studies (e.g., Burridge, 1973; Andrews, 1976; Das and Aki, 1977; Day, 1982; Madariaga and Olsen, 2000; Fukuyama and Olsen, 2002; Festa and Vilotte, 2006; Dunham, 2007; Liu and Lapusta, 2008; Shi et al., 2008; Lapusta and Liu, 2009). Based on an earlier analytical work of Burridge (1973), Andrews (1976) numerically showed that supershear transition can be produced by nucleating a daughter crack at the *S* wave shear stress

* Corresponding author. Now at Institute of Geophysics and Planetary Physics, Scripps Institution of Oceanography, University of California - San Diego.
E-mail address: ykaneko@ucsd.edu (Y. Kaneko).

0040-1951/$ – see front matter © 2010 Elsevier B.V. All rights reserved.
doi:10.1016/j.tecto.2010.06.015

peak ahead of the Mode II main rupture on faults governed by a linear slip-weakening friction law (Fig. 1) in which friction linearly decreases from static strength τ^s to dynamic strength τ^d over a characteristic slip d_c. This mechanism of supershear transition is often called 'the Burridge–Andrews mechanism.'

For the Burridge–Andrews mechanism of the supershear transition to occur on homogeneously prestressed faults in 2-D models, the level of prestress defined as $\bar{\tau}^o = (\tau^o - \tau^d)/(\tau^s - \tau^d) = 1/(1+S)$ must be high enough (i.e., $\bar{\tau}^o > \bar{\tau}^o_{crit} = 0.36$). Equivalently, the seismic ratio S defined as $S = (\tau^s - \tau^o)/(\tau^o - \tau^d)$ must be smaller than the critical value, $S_{crit} = 1.77$. Recently, Dunham (2007) showed that the critical level of prestress on homogeneously prestressed faults in 3-D models is given by $\bar{\tau}^o_{crit} = 0.46$ or, equivalently, $S_{crit} = 1.19$. This means that 3-D models generally require much larger prestress to allow the Burridge–Andrews mechanism to occur than 2-D models do (Day, 1982; Fukuyama and Olsen, 2002; Dunham, 2007).

Since the work of Burridge (1973) and Andrews (1976), a number of theoretical and numerical studies have addressed the issue of sub-Rayleigh-to-supershear transition on faults with non-uniformly distributed prestress or strength (e.g., Day, 1982; Olsen et al., 1997; Fukuyama and Olsen, 2002; Dunham et al., 2003; Liu and Lapusta, 2008; Lapusta and Liu, 2009). Under such circumstances, sub-Rayleigh-to-supershear transition and the subsequent supershear propagation can sometimes occur under background prestress levels that are lower than the ones predicted by the Burridge–Andrews mechanism. Examples include sub-Rayleigh rupture propagating into a region of increased stress drop (Fukuyama and Olsen, 2002) or a region of pre-existing quasi-statically expanding secondary crack (Liu and Lapusta, 2008), or sub-Rayleigh rupture breaking a strong heterogeneity on a fault (Dunham et al., 2003; Lapusta and Liu, 2009). Liu and Lapusta (2008) showed that the Burridge–Andrews mechanism belongs to a general case of sub-Rayleigh-to-supershear transition that subjects secondary cracks to a supershear loading field between the *S*-wave peak and earliest *P* waves propagating in front of a spontaneously expanding Mode II crack. Here we refer to such transition mechanism as 'the generalized Burridge–Andrews mechanism.' Heterogeneities in prestress and fault friction properties, therefore, play an important role on whether a rupture speed does or does not transition to a supershear speed and on its transition distance, i.e., the distance between the location of the hypocenter and the location of supershear transition.

Heterogeneities on natural faults that can potentially influence earthquake rupture speeds and induce transition to supershear speeds include the presence of the free surface and the variations in stress with depth. Supershear rupture propagation near the free surface has been reported in a number of simulations of spontaneous dynamic ruptures (Olsen et al., 1997; Aagaard et al., 2001; Day et al., 2008; Kaneko et al., 2008; Olsen et al., 2008). In particular, Olsen et al. (1997) noted that, in a dynamic rupture simulation of the 1992 Landers earthquake, supershear rupture propagation at shallow depths is caused by the free surface, which promotes "the generation of *S* to *P* converted head waves." However, supershear transition at shallow depth and its consequences for dynamic rupture have not been explored in more detail. This is because near-surface transition to supershear speeds has been mostly treated as an inconvenience to be avoided in numerical simulations, in the light of the general observations that most ruptures remain subshear. However, accumulating evidence suggests that most large strike-slip earthquakes have supershear speeds over parts of the fault rupture.

In this work, we explore the details of supershear transition induced by the free surface using simulations of spontaneous dynamic rupture on a vertical strike-slip fault embedded in an elastic half-space. We find two types of supershear transition mechanisms that can potentially act in the shallow portions of natural faults: one caused by the generalized Burridge–Andrews mechanism and the other related to the combined supershear loading fields generated by (a) the geometric effect of the rupture arrival at the free surface and (b) the free-surface phase conversion. To understand supershear rupture generation next to the free surface, we create several scenarios that remove one of more of these effects. As a result, we show that the additional stress field produced by the phase conversion of *SV* to *P*-diffracted waves at the free surface plays a key role in sustained supershear propagation next to the free surface (Section 5). Finally, we discuss the resulting global supershear transition over the entire fault depth and conditions and fault properties that favor or diminish the effectiveness of the supershear transition next to the free surface (Section 6).

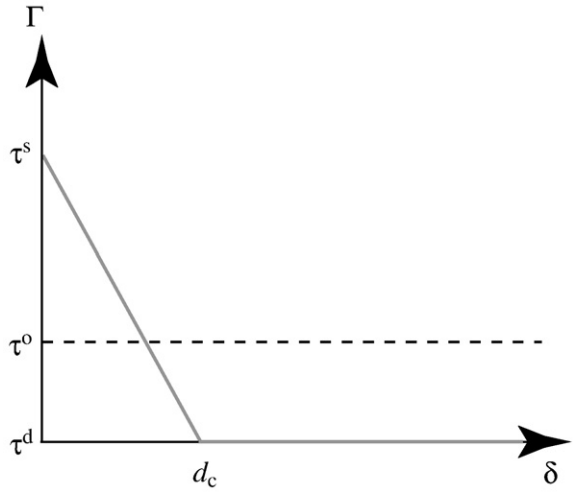

Fig. 1. Linear slip-weakening friction law. Γ is the frictional shear strength and δ is slip across the fault surface.

2. Fault models and parameters

We simulate dynamic rupture scenarios on a vertical strike-slip fault embedded into an elastic half-space (Fig. 2) with the *P*-wave speed of 6.0 km/s and *S*-wave speed of 3.46 km/s. The fault is governed by a linear slip-weakening friction law (Ida, 1972; Palmer and Rice, 1973), where its shear strength Γ linearly decreases from its static value τ_s to the dynamic value τ^d over the a characterize slip d_c:

$$\Gamma(\delta) = \begin{cases} \tau^d + (\tau^s - \tau^d)(1 - \delta/d_c), & \delta \le d_c, \\ \tau^d, & \delta > d_c. \end{cases} \quad (1)$$

The static strength τ_s and dynamic strength τ_d can be thought of as the products of time-independent effective normal stress $\bar{\sigma}$ and static and dynamic friction coefficients, respectively.

We solve the elastodynamic equation coupled with the friction law (1) using a spectral element method (Ampuero, 2002; Kaneko et al., 2008). Spectral element methods combine the flexibility of finite element methods with high numerical accuracy due to the use of higher-order Lagrange interpolants on Gauss–Lobatto–Legendre points that mimic the behavior of the Legendre basis (Komatitsch and Vilotte, 1998; Komatitsch and Tromp, 1999). On the fault, both strike and dip components of slip and shear traction are solved for numerically, i.e., rake rotation is allowed during slip. Absorbing conditions are used for all boundaries of the model domain except the free surface, to mimic a semi-infinite elastic half-space. The dynamic rupture code we use has been validated through the Southern California Earthquake Center Dynamic Earthquake-Rupture Code Validation Exercise (Harris et al., 2009).

Fig. 2 and Table 1 give model parameters and initial conditions. Unless noted otherwise, the time-independent effective normal stress $\bar{\sigma} = \min[1.0 + 16.2z, 120.0]$ MPa, where z is in kilometers, increases

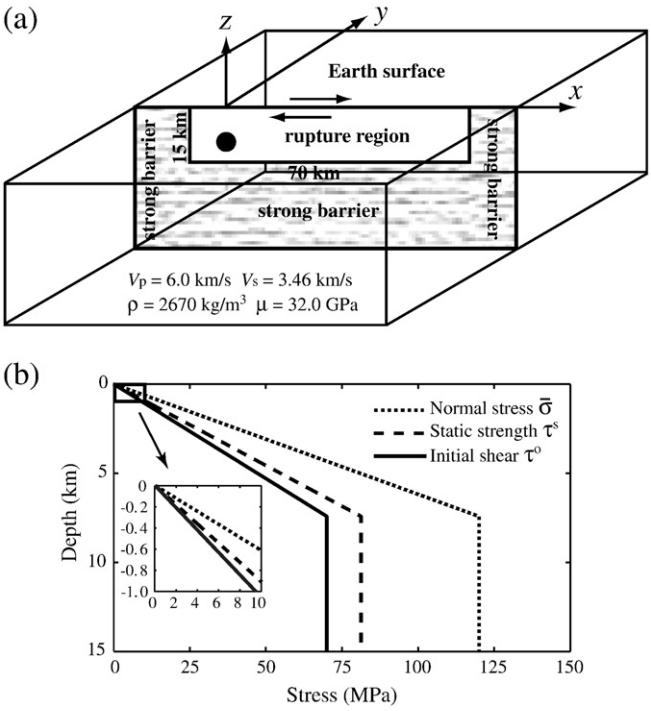

Fig. 2. (a) A 3-D model of a vertical strike-slip fault embedded into a linear elastic half-space. The slip-weakening (rupture) region is surrounded by unbreakable barriers. The black circle depicts a nucleation patch, where shear-stress perturbation is applied to initiate spontaneous dynamic rupture. (b) Depth-variable distribution of the effective normal stress $\overline{\sigma}$, static strength τ^p, and initial shear stress τ^o. Note that the nondimensional prestress ($\overline{\tau}^o$) and the seismic ratio S are uniform over the rupture region.

with depth due to the difference of overburden minus hydrostatic pore pressure and becomes constant (120.0 MPa) at depths larger than 7.4 km, due to the assumption that fluid over-pressure prevents further increase of $\overline{\sigma}$ with depth (Rice, 1993; Ben-Zion and Rice, 1997). Both the initial shear stress τ^o and dynamic strength τ^d are assumed to be proportional to $\overline{\sigma}$ such that the nondimensional prestress, $\overline{\tau}^o = (\tau^o - \tau^d)/(\tau^s - \tau^d)$, is uniform over the fault. Within the rupture domain (Fig. 2a), stress and strength (i.e., τ^o, τ_s, and τ_d) do not vary with distance along the fault strike. The fault strength is assumed to be infinite in the surrounding barriers. The characteristic slip d_c in the friction law (1) is 0.4 m and uniform over the fault.

An important characteristics of numerical solutions to dynamic rupture problems is the resolution of a cohesive zone, i.e., the portion of the fault plane behind the crack tip where the shear stress decreases from its static value to its dynamic value (Ida, 1972). To properly resolve the cohesive zone, the ratio $\Lambda/\Delta x$ of the cohesive zone size Λ to the average node spacing Δx needs to be at least 3 to 5 (Day et al., 2005). We use $\Delta x = 50$ m, and the value of λ in a typical scenario is $\approx$500 m, resulting in $\Lambda/\Delta x > 5$ in our simulations.

Table 1
Stress and friction parameters used in simulations. The values marked with an asterisk are for the region of constant $\overline{\sigma}$ (Fig. 2b).

Parameters	Within rupture region
Initial shear stress τ_o, MPa	70.0*
Effective normal stress $\overline{\sigma}$, MPa	120.0*
Static friction coefficient μ_s	0.677
Dynamic friction coefficient μ_d	0.525
Static strength $\tau_s = \mu_s\overline{\sigma}$, MPa	81.24*
Dynamic strength $\tau_d = \mu_d\overline{\sigma}$, MPa	63.0*
Dynamic stress drop $\Delta\tau = \tau_o - \tau_d$, MPa	7.0*
Strength excess $\tau_s - \tau_o$, MPa	11.24*
Critical slip distance d_o, m	0.40

The medium is initially at rest and, starting at time $t = 0$, dynamic rupture is initiated by imposing a rapid but smooth time-dependent variation of the horizontal shear traction in a circular patch (Appendix A). This initiation procedure results in fast but gradual variations in slip velocity, producing stable numerical results (Rojas et al., 2009). Once initiated at the nucleation patch, the rupture spontaneously propagates until it encounters the regions of much higher strength (unbreakable barriers) at the 15-km depth and at the lateral distances of −10 km and 60 km, where slip terminates (Fig. 2a).

We use the notion of rupture arrival time at a point on the fault to track slip progression. Rupture arrival time at a fault point is defined here as the time at which the slip rate (or slip velocity) at that point first exceeds 1.0 mm/s. The results do not depend on that value as long as it is small enough to capture slip initiation.

3. Numerical simulations of supershear rupture propagation near the free surface

Fig. 3 shows snapshots of spontaneously propagating dynamic rupture and the emergence of the secondary rupture front next to the free surface that propagates with a supershear speed. Since the level of absolute prestress and resulting stress drop are relatively low at shallow depths, this supershear rupture is initially only local and has a relatively small peak slip velocity of 0.5 m/s compared to the main rupture front with its peak slip velocity of 5 m/s (the snapshot at $t = 8.5$ s Fig. 3a). However, as the supershear rupture propagates farther, the slip velocity at the supershear front grows to a value comparable to that at the main rupture front. Subsequently, the initially local supershear pulse leads to global supershear transition, i.e., supershear speeds over the entire seismogenic depths (the snapshot at $t = 15.5$ s in Fig. 3a). The level of the non-dimensional prestress ($\overline{\tau}^o = 0.38$) used for this case is lower than the theoretical threshold ($\overline{\tau}^o = 0.46$) for supershear transition in 3-D models with no free surface given by Dunham (2007). Hence the presence of the free surface favors supershear rupture transition.

To take a closer look at the supershear rupture propagation in Fig. 3a, we plot slip velocity evolution along the fault trace (Fig. 4). The plot also gives the S-wave and P-wave arrivals from the nucleation region given by

$$t_{s\,or\,p}^{app} = \sqrt{(x^2 + z_o^2)}\,/\,V_{s\,or\,p}\ , \qquad (2)$$

where x is the distance along the fault trace measured from the epicenter, z_o is the depth at the center of the nucleation patch, and V_s and V_p are the S- and P-wave speeds of the medium, respectively. On the linear scale (Fig. 4a), we identify the main supershear slip pulse corresponding to the supershear rupture in Fig. 3a. Note that the supershear pulse propagates with speeds faster than the apparent S-wave speed related to the S-wave arrivals from the depth (Eq. (2)). We also find earlier, weaker supershear slip that can be seen only on the logarithmic scale (Fig. 4b). The amplitude of this earlier supershear pulse (1–10 cm/s) is much smaller than that of the dominant supershear pulse (>0.5 m/s). The earlier supershear pulse propagates at a speed between the apparent S- and P-wave speeds. These slip pulses merge with each other as they propagate farther away from the epicenter ($x > 25$ km in Fig. 4b).

Note that we call the free-surface rupture supershear if it propagates faster than the apparent S-wave speed. Alternatively, one could define supershear rupture on the basis of the formation of local Mach fronts (Harsha Bhat, private communication, 2009). However, the Mach fronts form immediately after the rupture reaches the free surface because shear waves created at that moment fall behind the rupture front arriving from the depth due to the 3-D

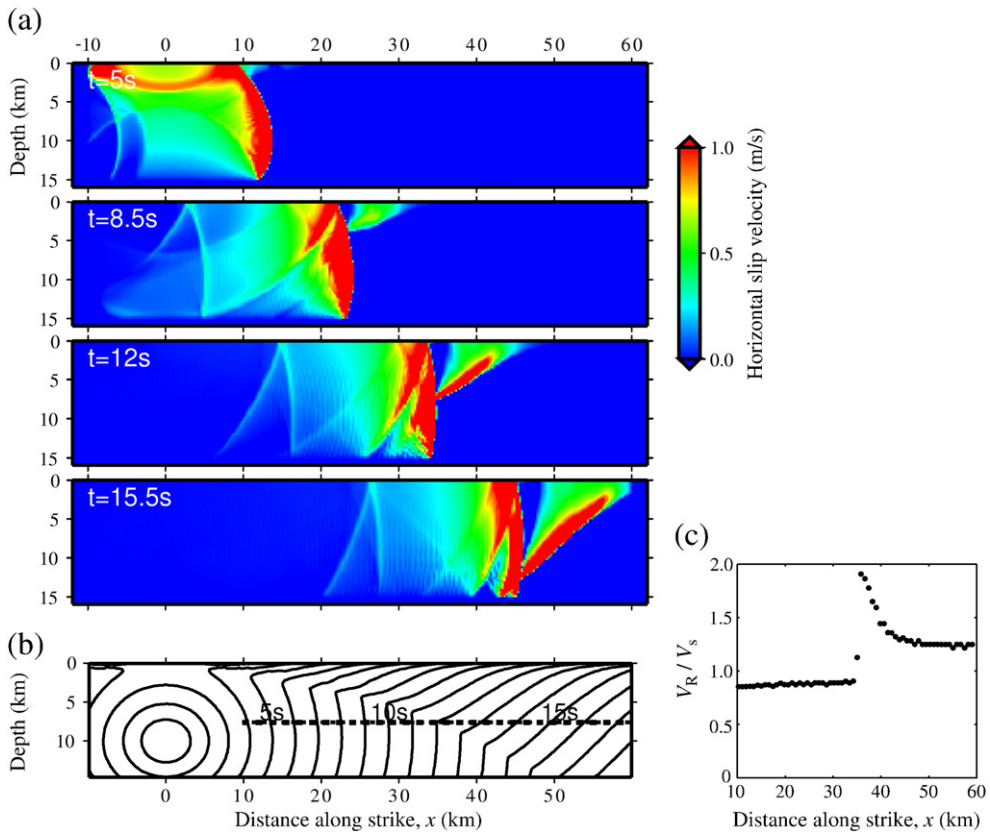

Fig. 3. (a) Snapshots of horizontal slip velocity on the fault every 3.5 s. The main rupture front propagates at sub-Rayleigh wave speeds. When the main rupture front reaches the free surface, supershear rupture is locally generated. This locally supershear rupture near the free surface ($t = 8.5$ s) causes global supershear transition ($t = 15.5$ s). The prestress level in this simulation ($\bar{\tau}^o = 0.38$) is lower than the theoretical threshold ($\bar{\tau}^o = 0.46$) for supershear transition in models with no free surface (Dunham, 2007). (b) Contours of rupture arrival times on the fault. The contours are plotted every 1 s. (c) Rupture speeds V_R along the mid-depth of the fault (horizontal dashed line in panel b) normalized by the *S*-wave speed V_s. At $x = 35$ km, the projected rupture speed jumps from sub-Rayleigh to supershear due to the arrival of the supershear rupture front at that depth.

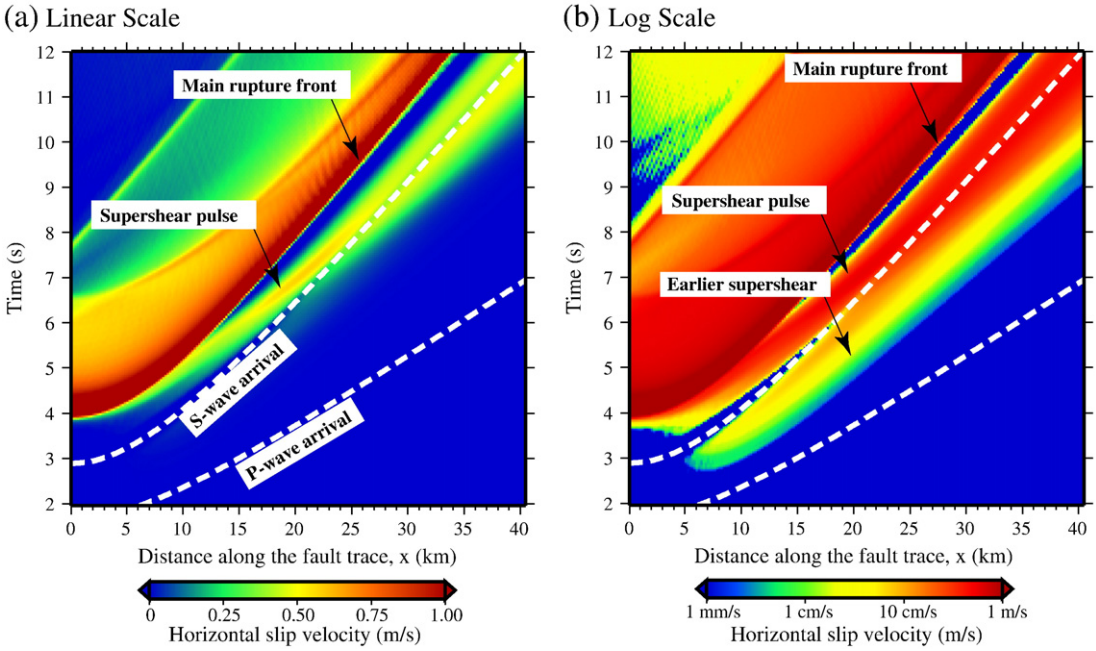

Fig. 4. (a) Space-time plot of horizontal slip velocity along the fault trace ($z = 0$ km). The dashed lines depict wave arrivals along the fault trace from the nucleation patch. Such wave arrivals define the apparent wave speeds along the fault trace. Ahead of the main rupture front, slip pulse with its amplitude of 0.5 m/s propagates faster than the apparent *S*-wave speed. (b) The same quantity as in panel a on a logarithmic scale. There are two distinct supershear rupture arrivals. Ahead of the dominant supershear pulse, there exists earlier supershear arrival with a smaller amplitude (1–10 cm/s).

geometrical effect. We adopt the supershear definition based on the apparent *S*-wave speed to ensure that what we call supershear rupture has faster rupture speeds than those that arise due to the geometrical effect (Fig. 4).

4. Origin of earlier, weaker supershear arrival: the generalized Burridge–Andrews mechanism of supershear transition

The weaker supershear arrival in Fig. 4b is caused by the generalized Burridge–Andrews mechanism of supershear transition. Fig. 5 illustrates the evolution of shear traction at different fault depths and how the earlier supershear slip is induced as a result of such transition mechanism. Once the main rupture front is initiated at the nucleation patch, a part of rupture front propagates towards the free surface. As the rupture front progresses into shallower depths, it propagates into the regions of relatively low absolute shear strength τ^s. Subsequently, the slip is induced by the loading field between the *P*-wave and *SV*-wave arrivals (Fig. 5d). This is consistent with findings by Liu and Lapusta (2008) that the stress loading field between the *P*-wave and *SV*-wave arrivals can produce supershear sliding in the presence of heterogeneities. On most of the fault, the supershear loading field is not sufficient for initiation of supershear rupture (Fig. 5b, c). Near the free surface, the earlier supershear pulse is induced due to low strength there relative to the depth (Fig.5d). Hence regions of low relative shear strength near the free surface act as a heterogeneity in our model.

To confirm that the earlier, weaker supershear arrival is caused by the supershear loading field, we consider the cases with uniform effective normal stress $\overline{\sigma}$, uniform initial stress τ^o, and uniform dynamic strength τ^d throughout the depth. Such conditions eliminate the relative strength difference between deeper and shallower regions, and we expect that the earlier, weaker supershear arrival would disappear as well. This is exactly what we find (Figs. 6a; 7a). Our results suggest that the emergence of the earlier, weaker supershear rupture depends strongly on the variation of strength and prestress with depth. For natural earthquakes, weaker supershear slip may occur near the fault trace. However, detecting or inferring such supershear rupture may be difficult due to its small amplitude. The resulting ground motion would be much smaller than that associated with the main subshear rupture front. In addition, such supershear rupture may be diminished on natural faults due to factors discussed in Section 6.

5. Origin of dominant supershear pulse: relation to phase conversion of *SV* to *P*-diffracted waves

Here we investigate the origin of the second, dominant supershear pulse (Fig. 4). To eliminate the earlier, weaker supershear slip and hence to focus on the dominant supershear rupture, we consider scenarios with uniform prestress in this section.

The dominant supershear pulse has several interesting properties distinct from the traditional Burridge–Andrews mechanism. First, the dominant supershear rupture next to the free surface is not nucleated from a daughter crack, or a secondary crack, ahead of the main rupture front. Rather, supershear pulse emerges from the main rupture front itself (Fig. 7a). Second, the transition distance depends on the depth of the nucleation patch (Fig. 7a, b). Transition distances (black dashed lines in Fig. 7) are found by superimposing the apparent *S*-wave arrival onto the rupture front and finding a location at which the speed of the rupture front first exceeds the apparent *S*-wave arrival for each case. Fig. 7a, b show that the case with a deeper nucleation patch leads to a longer transition distance. Third, the transition distance to near-surface supershear propagation is less sensitive to the levels of background prestress $\overline{\tau}^o$ or, equivalently, the seismic ratio *S* (Fig. 7, panels a, c, d). Slight variations in the transition distance

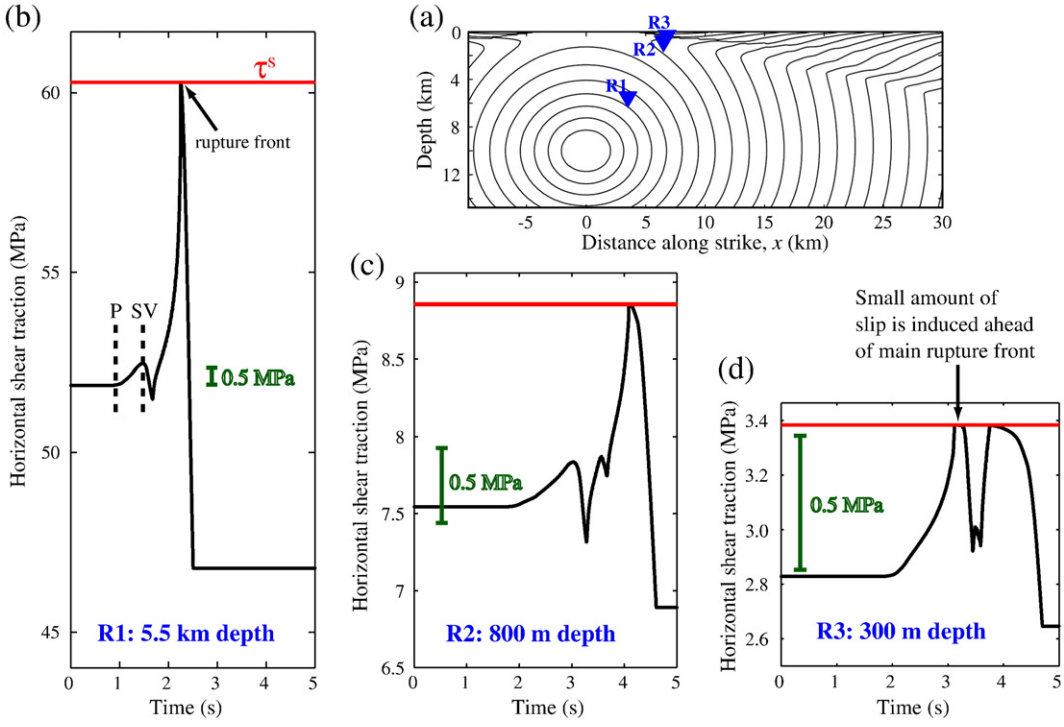

Fig. 5. Generalized Burridge–Andrews transition at the free surface. (a) Contours of rupture arrival times on the fault plotted every 0.5 s. (b–d) The magnitude of horizontal shear traction at receiver locations (R1–R3) shown in panel a. The receiver locations are chosen to be approximately parallel to the propagation direction of the main rupture front. Red lines correspond to the values of static strength τ^s at each receiver depth. The values decrease towards the free surface. This creates low strength near the free surface relative to the depth. At receiver R3, the shear stress peak between *P*-wave and *SV*-wave arrivals, which was relatively insignificant at depth, reaches τ^s and, as a result, slip is induced ahead of the main rupture front. This slip corresponds to the earlier, weaker supershear arrival shown in Fig. 4b.

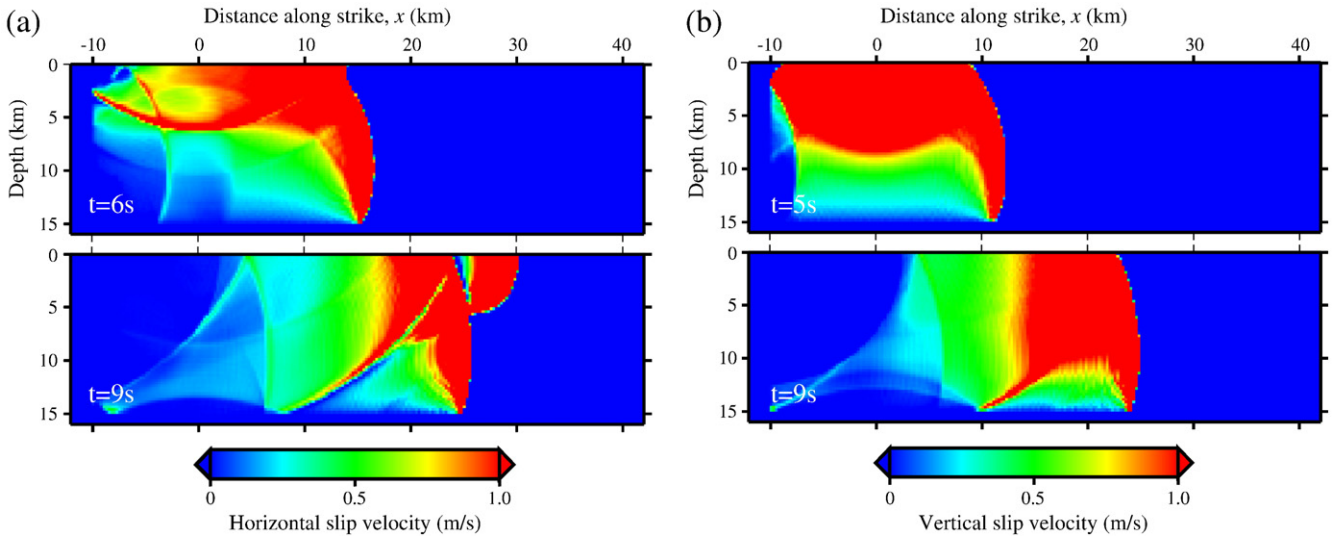

Fig. 6. (a) Snapshots of horizontal slip velocity for the case with uniform effective normal stress ($\overline{\sigma}$ = 120 MPa) over the fault. The nondimensional prestress is uniform over the fault and the same as in Fig. 3 ($\bar{\tau}^{rmo}$ = 0.38). Note that, at t = 6 s, the amplitude of slip velocity of the supershear rupture pulse (5–10 m/s) is much higher than that in the case with depth-dependent prestress (0.5–1 m/s). (b) Snapshots of vertical slip velocity for the case with vertical dip-slip faulting and uniform effective normal stress ($\overline{\sigma}$ = 120 MPa) over the fault. The magnitude of the nondimensional prestress is the same as in panel a ($\bar{\tau}^{o}$ = 0.38). No supershear rupture is generated next to the free surface.

in Fig. 7a, c, d are due to the different shapes of the rupture front for each case. The final point, related to the third property, is that supershear rupture induced by the free surface occurs at lower levels of the background prestress than the one predicted by the Burridge–Andrews mechanism and, in fact, appears to be nearly independent of the prestress level. Whether such local, near-surface, supershear transition can trigger global supershear transition over the entire seismogenic depth is discussed in Section 6.1.

There are two potential explanations for the near-surface supershear transition and propagation with such properties. One is the geometric effect of the rupture arrival at the free surface and the associated supershear loading field. As Fig.7a shows, the effective rupture speed in the direction of the free surface is infinite at the time of rupture arrival at the free surface, diminishing with time. While we do not count such rupture propagation as truly supershear, because the rupture speed is still below the arrivals of the shear waves themselves, this high-speed slip, amplified by the presence of the free surface, should generate a supershear loading field, as defined by Liu and Lapusta (2008). This stress field stays behind the crack front for a while, and would manifest itself after the effective speed of the rupture front along the free surface reduces below the *P*-wave speed. This explains the dependence of the transition distance on the depth of the nucleation and relative insensitivity of the transition distance to the prestress field, other than any effects the prestress field would have on the shape of the rupture front arriving from the depth at the free surface. The other important free-surface effect is the phase conversion of *SV* to *P*-diffracted waves (Appendix B). By generating additional *P*-waves, the phase conversion is expected to significantly enhance the supershear loading field and hence promote the supershear transition and propagation.

To analyze the relative importance of these effects, we consider a scenario based on the case of Figs. 6a and 7a, but without the free surface and with a mirror-image rupture. The image rupture is positioned so that the two ruptures collide with each other along the horizontal line $z=0$ (Fig. 8a). This mirror-image method retains the free-surface effect of rupture amplification. In fact, by comparing Fig. 7a with Figs. 8b, and 9c with d, we find that the two cases one with the free surface and the other with the mirror-image rupture have very similar evolution of the slip velocity and horizontal rupture speed at $z=0$, up until the emergence of supershear propagation. However, the case with the image rupture induces the following boundary conditions on the plane $z=0$: $\tau_{zx}=\tau_{zy}=0$ and displacement $u_z=0$, which are different from the conditions for a free surface ($\tau_{zx}=\tau_{zy}=\tau_{zz}=0$). This difference modifies phase conversions at the free surface.

We find that the case with the image rupture also produces local supershear rupture, but it is short-lived (Fig. 8b). Supershear transition occurs in the same place as for the case with the free surface, pointing to the importance of the amplified near-surface slip and the stress field it generates. At the same time, the supershear pulse dies in the case with the image rupture, showing the importance of phase conversion and the associated higher stress field for maintaining supershear propagation. To check that the case with the free surface indeed has larger along-strike shear stresses ahead of the rupture tip, we plot stresses in Figs. 8c, d and 9a, b. Note the difference in shear stress ahead of the rupture front within the black rectangles in Fig. 8c, d; this difference is explicitly plotted in Fig. 9a, b for one location within that rectangle. Simulations with the image rupture and different values of prestress show that the survival of the supershear rupture without the true free surface strongly depends on the prestress level, with sustained supershear propagation only possible for prestress levels close to the ones predicted by the Burridge–Andrews mechanism for homogeneous faults.

Hence we conclude that the dominant supershear pulse next to the free surface is caused by the combination of the amplified near-surface slip and the phase conversion of *SV* to *P*-diffracted waves. The phase conversion effect is needed to maintain the sustained near-surface supershear rupture for prestress levels lower than the ones predicted by the Burridge–Andrews transition mechanisms.

Note that the supershear transition due to a free surface has similarities with the generalized Burridge–Andrews mechanism discussed in Liu and Lapusta (2008). In both cases, (i) the transition is caused by rupture interaction with heterogeneity (in this case the free surface), (ii) the transition distance is determined by the properties of heterogeneity (in this case, how far the free surface is from the nucleation location) and not the prestress, and hence (iii) the supershear transition and propagation can occur at levels of prestress lower than the one for the traditional Burridge–Andrews mechanism. An important difference of the free-surface transition in comparison with the cases considered in Liu and Lapusta (2008) is that no secondary crack is generated. In the generalized Burridge–Andrews

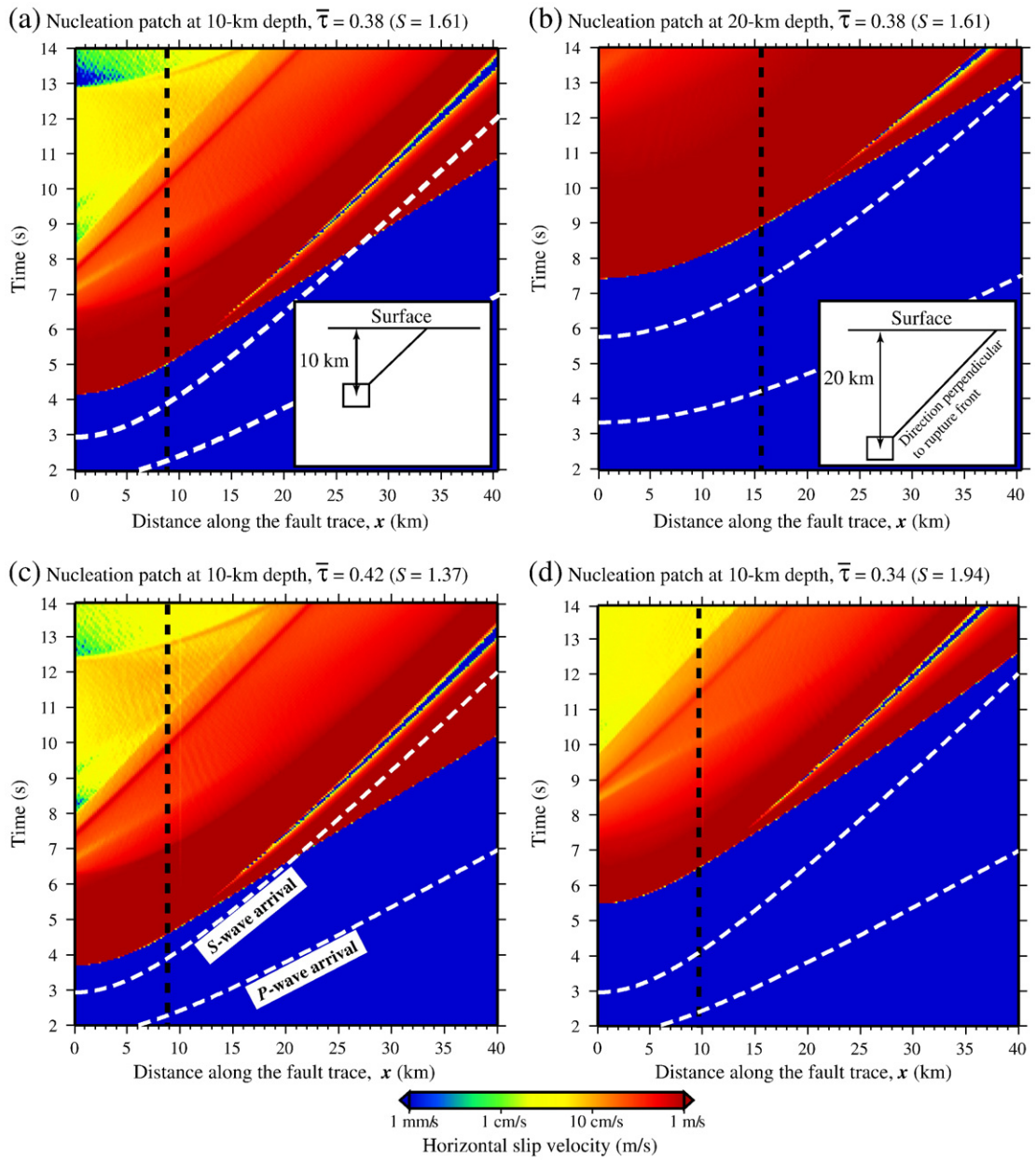

Fig. 7. (a) Space-time plot of horizontal slip velocity along the fault trace ($z = 0$ km) for the case with uniform effective normal stress ($\overline{\sigma}$ = 120 MPa) over the fault. The same logarithmic scale as in Fig. 4b is used. White dashed lines depict wave arrivals along the fault trace from the nucleation patch. A black dashed line approximately corresponds to the location of the subshear-to-supershear transition as discussed in the main text. The rupture speed of the supershear pulse is approximately 5.3 km/s. Note that earlier weaker supershear arrival is not present because there is no relative difference in fault strength with depth. (b) The case with the nucleation patch placed at 20-km depth. The subshear-to-supershear transition distance increases as the depth of the nucleation patch increases, consistent with the phase-conversion mechanism. (c) The case with larger prestress ($\overline{\tau}$ = 0.42; S = 1.37). (d) The case with lower prestress ($\overline{\tau}$ = 0.34; S = 1.94). The transition distance resulting from the phase conversion at the free surface is independent of the level of prestress in the range of the parameters shown here.

mechanism as defined by Liu and Lapusta (2008), supershear transition occurred due to the interaction of the stress field of the main rupture with secondary ruptures or cracks generated by heterogeneities in front of the main rupture. In the case of the dominant supershear rupture at the free surface, the tip of the main rupture itself transitions to supershear speeds due to interaction with the stress field generated by the near-surface sliding behind the rupture front and by phase conversion along the free surface.

Simulations with vertical dip-slip faulting do not result in supershear rupture next to the free surface (Fig. 6b). This is consistent with the zero additional shear stress produced by *P*-waves in the mode III directions, including P-diffracted waves which have zero vertical component along the free surface (Appendix B).

6. Factors that affect supershear transition due to the free surface

Given that global supershear rupture transition related to phase conversion can occur under a wide range of prestress conditions, it is important to understand whether such supershear rupture transition and subsequent supershear propagation would be favored on natural faults. As we discuss in the following, there are several potentially important factors on natural faults that can influence the effectiveness of such transition.

6.1. Larger prestress and transition to global supershear propagation

In Section 5, we find that, for the phase-conversion mechanism, the supershear transition distance for local transition at the free surface is

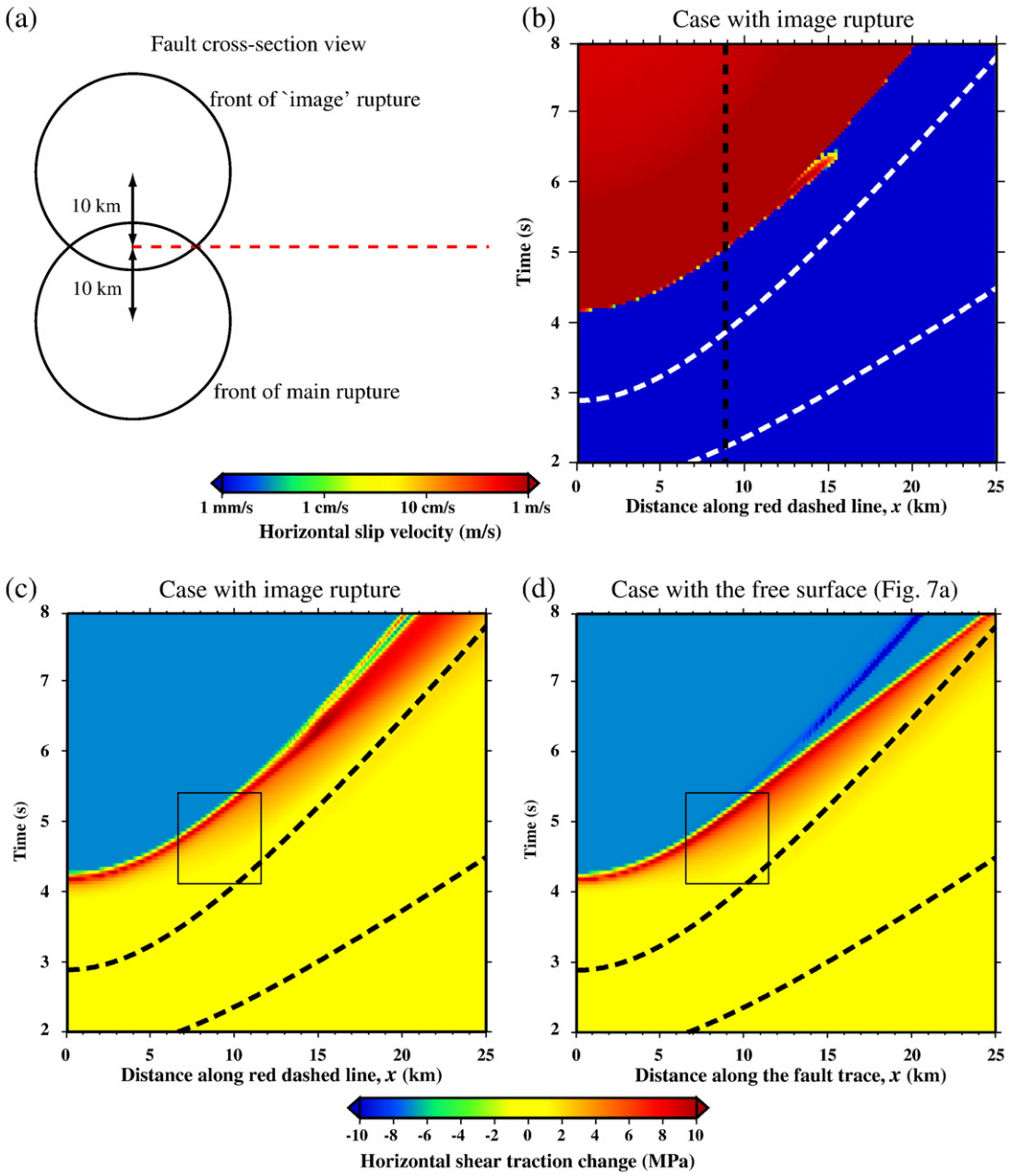

Fig. 8. (a) A sketch illustrating the main rupture front interfering with the image rupture front on a fault embedded in an infinite space. (b) Space-time plot of horizontal slip velocity along the red dashed line shown in panel a for the case with the image rupture. Supershear rupture is produced, but it is transient and disappears after a short propagation distance (≈6 km). (c–d) Space-time plot of horizontal shear traction change along the dashed line shown in panel a for the cases with image rupture (panel c) and with the free surface (panel d). The amount of shear stress increase ahead of the rupture front at around the transition distance (≈9 km) is higher in the case with the free surface than that with the image rupture. Black and white dashed lines in panels b–d have the same meaning as in Fig. 7.

independent of the level of the prestress. In the more realistic cases with depth-dependent effective normal stress, this conclusion still holds (Fig. 10). However, whether this local supershear propagation turns into global supershear rupture, with supershear speeds over the entire seismogenic depth, and the distance at which this occurs, does depend on the level of prestress and hence the seismic ratio S. For example, the case with $\bar{\tau}^0 = 0.42$ in Fig. 10 results in global supershear transition at about $x = 40$ km, whereas in the case with $\bar{\tau}^0 = 0.38$, global supershear transition occurs at about $x = 50$ km. The case with $\bar{\tau}^0 = 0.34$ in Fig. 10 has no global supershear transition although the rupture speed is locally supershear next to the free surface. Hence the global supershear transition depends on the background levels of prestress, whereas local supershear transition related to phase conversion does not. Larger levels of background prestress promote the propagation of the global supershear rupture.

Note that the levels of background prestress in all the cases considered in Fig. 10 are lower than the theoretical threshold for global supershear propagation ($\bar{\tau}^0 = 0.46$) for models with no free surface (Dunham, 2007). This means that, on homogeneously prestressed faults, global supershear transition resulting from the local supershear rupture next to the free surface does not require the level of prestress predicted by the Burridge–Andrews mechanism. On natural faults, this condition may not hold since distributions of stress/strength heterogeneities over the fault surface can strongly control the occurrence of supershear transition and subsequent propagation by the generalized Burridge–Andrews mechanism.

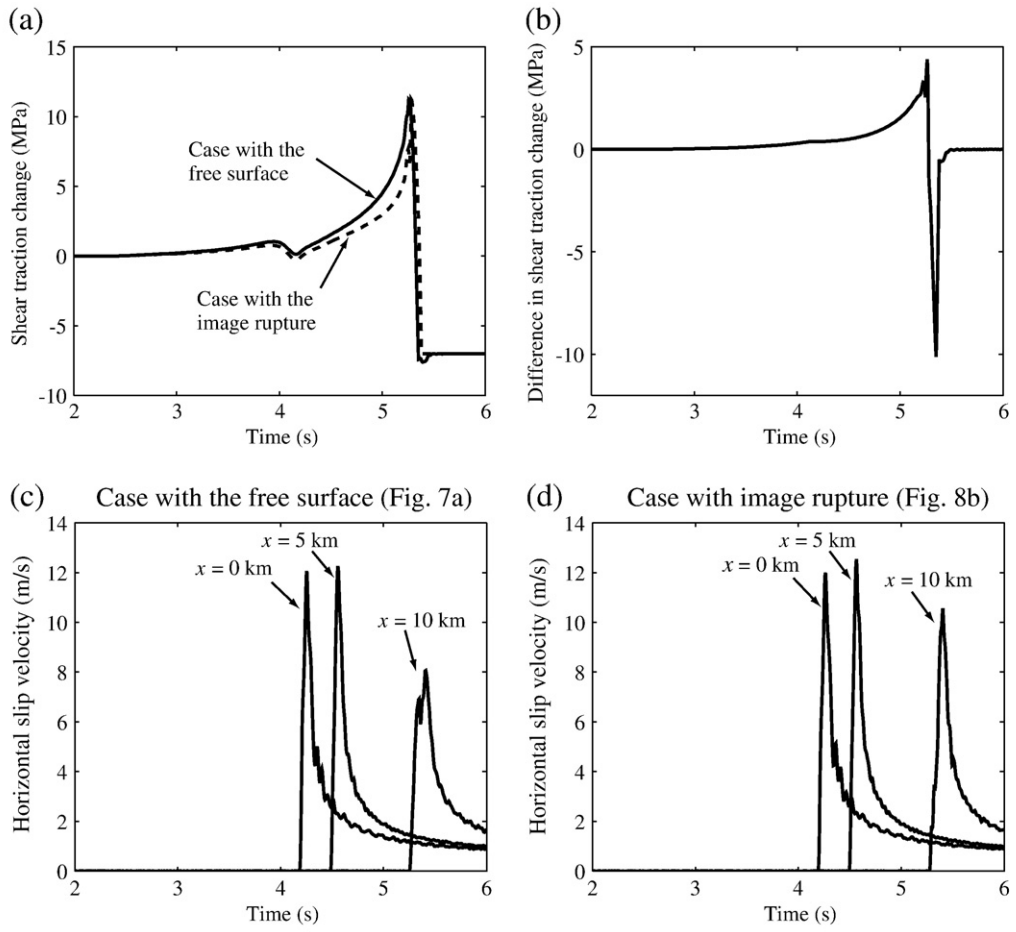

Fig. 9. (a) The magnitude of horizontal shear traction change at a receiver (x, z) = (10, 0) km for the cases with the image rupture and with the free surface. The shear traction is noticeably higher in the case with the free surface, creating sustained supershear rupture propagation shown in Fig. 7a. (b) The difference between the solid and dashed lines in panel a. (c–d) Horizontal slip velocity at three receiver locations ($x = 0, 5, 10$ km and $z = 0$ km) for the cases with the free surface (panel c) and with the image source (panel d). The kinematics of these two cases is similar up until the stronger supershear rupture emerges in the case with the free surface.

6.2. Shallow layers of lower wave speeds

Sedimentary basins are commonly found along major plate boundaries and mature faults. To study their effect, we analyze how low-velocity bulk layers at shallow depths affect supershear transition next to the free surface and subsequent rupture propagation. Fig. 11 gives wave speeds used for the layered bulk structure. As the radiating SV waves propagate through regions of lower-velocity bulk at shallow depths, the wave front curvature changes, and the resulting incidence angle becomes smaller as the SV wave progresses toward the free

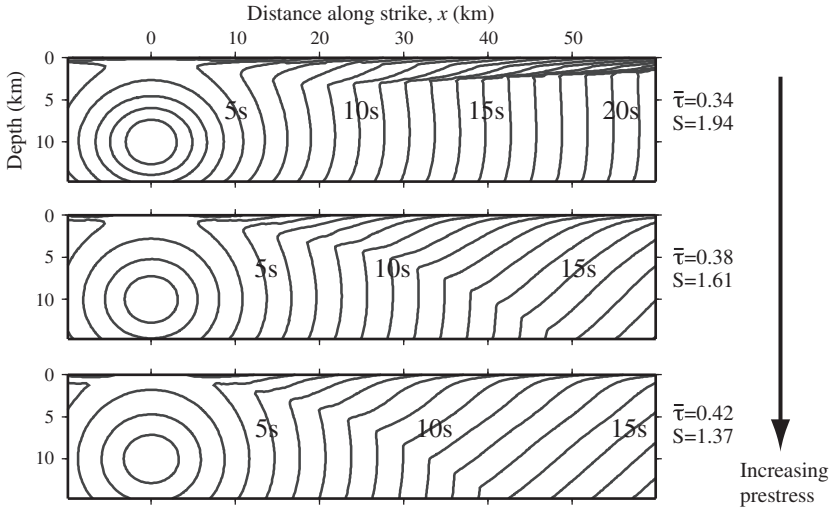

Fig. 10. Effect of prestress on supershear rupture propagation for cases with depth-dependent effective normal stress. For each case, the value of prestress used is indicated. The contours of rupture-front arrival times are plotted every 1 s. Larger prestress promotes the propagation of global supershear rupture.

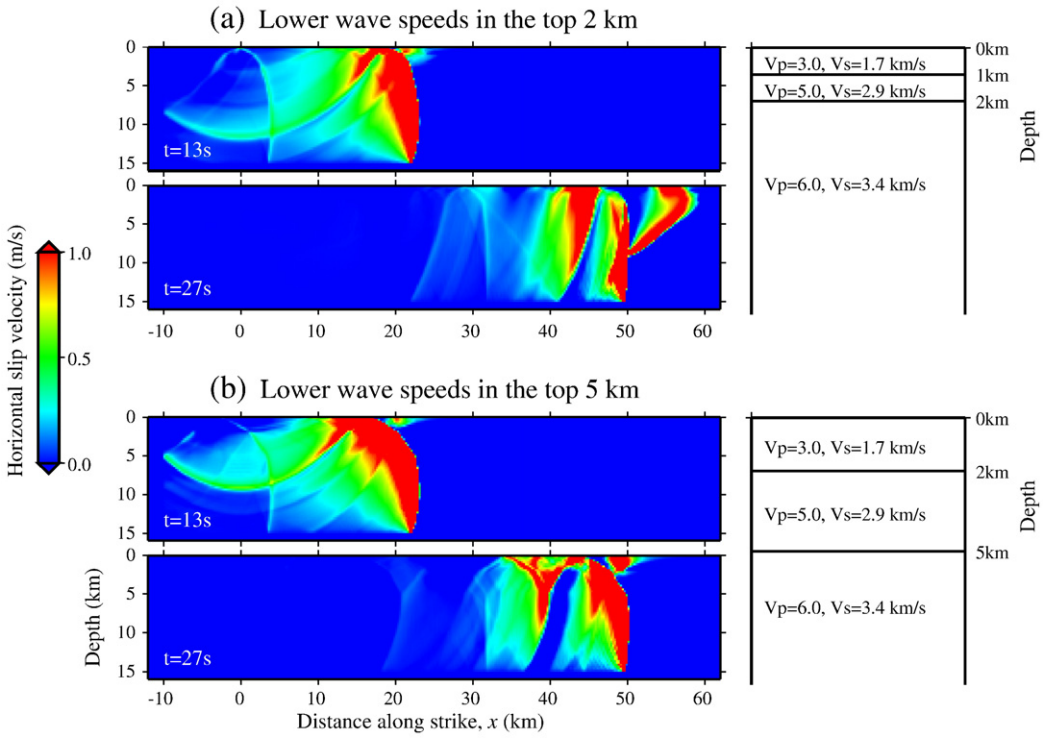

Fig. 11. Snapshots of horizontal slip velocity for the case with the layered bulk structure and depth-dependent effective normal stress across the fault. (a) Two low-velocity bulk layers are placed within the top 2 km. The elastic wave speeds and thickness of each layer are indicated. In the presence of shallow low-velocity layers, the supershear rupture speed near the surface can be slower than the sub-Rayleigh rupture speed at depths ($t = 13$ s). The global supershear transition distance here becomes larger than that with the homogeneous bulk (Fig. 3a). (b) The case with lower wave speeds in the top 5 km. The presence of shallow layers of lower wave speeds diminish the effectiveness of global supershear transition.

surface. This diminishes the supershear transition related to phase conversion to some extent, although it can still occur (Fig. 11a, b). However, the supershear rupture speed on the shallow portion of the fault is slower than the sub-Rayleigh rupture speed at depths in our example (Fig. 11). Additionally, the presence of the shallow layers of low-velocity materials substantially diminishes the effectiveness of the global supershear transition (Fig. 11a, b). Hence, global supershear transition related to phase conversion is sensitive to the bulk velocity structure. If the bulk velocity structure is relatively homogeneous over the seismogenic depth, e.g. for faults that bisect mainly hard rocks such as granite at shallow depths, global supershear rupture due to the free surface may occur under a wide range of stress conditions as shown in Fig. 10.

6.3. Velocity-strengthening fault friction at shallow depths

Accumulating evidence supports the presence of velocity-strengthening fault friction at shallow depths. In laboratory experiments, rock friction at low normal stress typically exhibits velocity-strengthening behavior due to unconsolidated fault gouge (e.g., Marone et al., 1991; Marone, 1998). Theoretical studies have shown that velocity-strengthening friction responds to loading with stable sliding and does not allow for spontaneous nucleation of frictional instabilities (Ruina, 1983; Rice and Ruina, 1983). Hence shallow afterslip of large earthquakes (e.g., Marone et al., 1991; Marone, 1998; Hsu et al., 2006) and the deficit of seismicity at shallow depths (e.g., Shearer et al., 2005) provide indirect observational evidence for velocity-strengthening fault rheology at shallow depths.

If the friction rheology in the shallow portions of natural faults is substantially velocity strengthening, the propagation of supershear rupture next to the free surface can be diminished (Kaneko et al., 2008). On the one hand, this is consistent with the fact that supershear rupture propagation near the free surface has not been commonly reported in large crustal earthquakes. On the other hand, during earthquakes with inferred supershear speeds, fault segments that had supershear rupture speeds also had large surface offset (e.g., Haeussler et al., 2004; Vallée et al., 2008). Therefore, there may be a connection between supershear ruptures and friction properties of the shallow fault portions. Lateral variations in friction rheology may exist such that the fault segments with velocity-weakening shallow portions are the ones that experience supershear ruptures, with local near-surface supershear rupture leading to global supershear transition and subsequent supershear propagation.

6.4. Off-fault plasticity and damage

Geological observations of the structure of mature faults indicate that the typical fault zone consists of finely granulated materials surrounded by a gouge layer and damaged or fractured host rock (e.g., Chester et al., 1993). Several studies suggested that inelastic off-fault response during rupture propagation can limit the peak slip velocity at the rupture front and/or delay or prevent supershear rupture propagation (e.g., Yamashita, 2000; Andrews, 2005; Duan and Day, 2008; Ma, 2008; Templeton and Rice, 2008). Since the confining pressure is relatively low near the surface, the inelastic zone can broaden at shallow depths (Ma, 2008; Finzi et al., 2009). If the inelastic response becomes progressively important at shallow depths, such response is likely to diminish the effectiveness of local supershear transition due to the free surface. Understanding supershear transition due to the free surface combined with inelastic response remains a subject for future research.

7. Conclusions

We have analyzed the occurrence of supershear transition induced by the free surface using simulations of spontaneous dynamic rupture

on a fault governed by a linear slip-weakening friction law. We have shown that locally supershear rupture near the free surface can occur due to (i) the supershear loading field between *P*- and *SV*-wave arrivals radiated by rupture propagation at depths, and (ii) the supershear loading field caused by the amplified slip and phase conversion of *SV* to *P*-diffracted waves at the free surface. The earlier, weaker supershear slip due to (i) is caused by low normal stress and hence low strength at shallow portions of the fault relative to the deeper parts. The dominant supershear rupture due to (ii) is relatively insensitive to the levels of the background prestress or, equivalently, the seismic ratio, and occurs in all cases that we considered.

Such locally supershear rupture can cause global supershear transition, with the rupture speed becoming supershear over the entire seismogenic depth. The global transition does depend on the level of background prestress although it can occur under prestress lower than the theoretical estimates for models with no free surface. The transition distance of the global supershear rupture is shorter for larger levels of background prestress, and hence larger prestress favors propagation of the global supershear rupture.

To understand the applicability of such supershear transition to natural earthquakes, we have analyzed factors that may control the effectiveness of this transition. The effectiveness of supershear transition near the free surface on natural faults can be diminished by a number of potentially important factors, including shallow layers of lower wave speeds, shallow fault regions of velocity-strengthening friction, and off-fault plasticity and damage. In addition, kinematic and dynamic rupture inversions of earthquakes often show complex rupture histories, with rupture propagating down-dip and up-dip during large strike-slip earthquakes (e.g., Heaton, 1990; Olsen et al., 1997), which may further modify the effectiveness of supershear transition next to the free surface, either decreasing or amplifying it. However, supershear transition induced by the free surface may still be the cause of some supershear earthquakes, given that many of the reported supershear earthquakes resulted in large surface offset along the supershear segment, which would lead to supershear transition related to phase conversion at least locally.

Acknowledgements

This study was supported by the National Science Foundation (grant EAR0548277) and the Southern California Earthquake Center (SCEC). SCEC is funded by NSF Cooperative Agreement EAR-0106924 and USGS Cooperative Agreement 02HQAG0008. The SCEC contribution number for this paper is 1324. The numerical simulations for this research were performed on Caltech Division of Geological and Planetary Sciences Dell cluster. We thank Don Helmberger, Daoyuan Sun, and Steve Day for helpful discussions.

Appendix A. Rupture initiation procedure

To nucleate dynamic rupture, we need to abruptly increase slip velocity from zero to coseismic values (~1 m/s). To achieve this numerically, we use a perturbation of shear stress that smoothly grows from zero to its maximum amplitude $\Delta\tau_o$ over a finite time interval T and is confined to a finite circular region of the fault of radius R. Following the approach used in Rojas et al. (2009), we apply a horizontal shear traction perturbation of the form:

$$\Delta\tau(x,z,t) = \Delta\tau_o F(\sqrt{(x-x_o)^2 + (z-z_o)^2})G(t), \tag{A.1}$$

where

$$F(r) = \begin{cases} exp\left[r^2/(r^2-R^2)\right] & \text{if } r<R \\ 0 & \text{if } r\geq R \end{cases}, \tag{A.2}$$

and

$$G(t) = \begin{cases} exp\left[(t-T)^2/(t^2-2tT)\right] & \text{if } 0<t<T \\ 1 & \text{if } t\geq T \end{cases}. \tag{A.3}$$

The perturbation is radially symmetric, with the radial distance away from the hypocenter along the fault given by $r = \sqrt{(x-x_o)^2 + (z-z_o)^2}$. We use $R = 2.5$ km, $\Delta\tau_o = 15.0$ MPa, and $T = 0.1$ s.

Appendix B. Phase conversion of *SV* to *P*-diffracted waves

Here we give analytical expressions for phase conversion of *SV* to *P*-diffracted plane waves at a free surface. Vector displacements involved in *SV*-*P* plane-wave problems can be found in Aki and Richards (2002, pp. 128–139). The upgoing *SV* wave with amplitude *S* is given by

$$S(\cos j, 0, \sin j)exp\left[i\omega\left(\frac{\sin j}{V_s}x - \frac{\cos j}{V_s}z - t\right)\right] \tag{B.1}$$

where ω is the angular frequency of the plane wave, and j is an angle defined in terms of the ray trajectories, orthogonal to the plane fronts of *SV*. In the case of an *SV*-wave incident on the free surface, we can expect a reflected *P* wave and a reflected *SV* wave. Vector displacements of these reflected waves due to a free surface boundary are given by

$$S(\sin i, 0, \cos i)SP\, exp\left[i\omega\left(\frac{\sin i}{V_p}x + \frac{\cos i}{V_p}z - t\right)\right] \tag{B.2}$$

for down-going *P*, and

$$S(\cos j, 0, -\sin j)SS\, exp\left[i\omega\left(\frac{\sin j}{V_s}x + \frac{\cos j}{V_s}z - t\right)\right] \tag{B.3}$$

for down-going *SV*, where i in front of the angular frequency ω is the imaginary number (i.e., $i = \sqrt{-1}$), whereas i in other places represents the angle orthogonal to the plane fronts of the converted

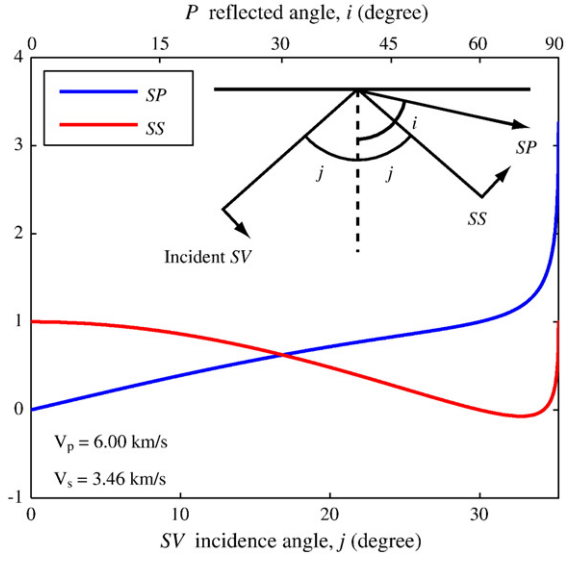

Fig. 12. The *SV*-*P* and *SV*-*SV* conversion coefficients (displacement amplitude ratios) for a free surface. Conversion coefficients *SP* and *SS* are given in Eqs. (B.4) and (B.5), respectively. We set $V_p = 6$ km/s and $V_s = 3.46$ km/s. In the inset, notation and sign convention for coefficients due to *SV* incidence on a free surface are shown. A motion is taken as positive if its component to the right (i.e., in the horizontal direction of propagation) has the same phase as the propagation factor $exp[i\omega(px-t)]$. At the critical angle (i.e., $i = 90^o$), *SP* is quite large (≈ 3.3).

P wave (Fig. 12). SP and SS are conversion coefficients given by Eqs. (5.31) and (5.32) of Aki and Richards (2002):

$$SP = \frac{4\frac{V_s}{V_p} p \frac{\cos j}{V_s}\left(\frac{1}{V_s^2} - 2p^2\right)}{\left(\frac{1}{V_s^2} - 2p^2\right)^2 + 4p^2 \frac{\cos i}{V_p}\frac{\cos j}{V_s}}, \tag{B.4}$$

$$SS = \frac{\left(\frac{1}{V_s^2} - 2p^2\right)^2 - 4p^2 \frac{\cos i}{V_p}\frac{\cos j}{V_s}}{\left(\frac{1}{V_s^2} - 2p^2\right)^2 + 4p^2 \frac{\cos i}{V_p}\frac{\cos j}{V_s}}, \tag{B.5}$$

where $p = \frac{\sin i}{V_p} = \frac{\sin j}{V_s}$ is the ray parameter.

Fig. 12 shows conversion coefficients as functions of the incidence angle of SV plane wave. At the critical angle ($j = 35.3°$ for the elastic properties considered, $i = 90°$), the P-diffracted wave (or the head wave) propagates along the free surface. The amplitude of the P-diffracted wave is 3.3 times higher than that of the incident SV wave (Fig. 12). Such amplification factors suggest that phase conversion of incident SV waves radiated by the main subshear rupture coming from the depth of the fault should cause significant increase in the supershear loading field next to the free surface, promoting sustained supershear rupture propagation. Note that the vertical component of the P-diffracted wave is zero along the free surface because $\cos i$ in Eq. (B.2) becomes zero, which explains why the P-diffracted waves do not cause near-surface supershear transition in the dip-slip case.

References

Aagaard, B.T., Heaton, T.H., 2004. Near-source ground motions from simulations of sustained intersonic and supersonic fault ruptures. Bull. Seismol. Soc. Am. 94 (6), 2064–2078.

Aagaard, B.T., Heaton, T.H., Hall, J.F., 2001. Dynamic earthquake ruptures in the presence of lithostatic normal stresses: implications for friction models and heat production. Bull. Seismol. Soc. Am. 91 (6) 11,765-11,796.

Aki K., Richards P.G., 2002. University Science Books, Sausalito, California.

Ampuero J.-P., 2002. Etude physique et numérique de la nucléation des séismes. Ph.D. thesis, Univ. Paris 7, Denis Diderot, Paris.

Andrews, D.J., 1976. Rupture velocity of plane strain shear cracks. J. Geophys. Res. 81, 5679–5687.

Andrews, D.J., 2005. Rupture dynamics with energy loss outside the slip zone. J. Geophys. Res. 110.

Archuleta, R.J., 1984. A faulting model for the 1979 imperial valley earthquake. J. Geophys. Res. 89, 4559–4585.

Ben-Zion, Y., Rice, J.R., 1997. Dynamic simulations of slip on a smooth fault in an elastic solid. J. Geophys. Res. 102 17,771-17,784.

Bernard, P., Baumont, D., 2005. Shear Mach wave characterization for kinematic fault rupture models with constant supershear rupture velocity. Geophys. J. Int. 162, 431–447.

Bhat, H.S., Dmowska, R., King, G.C.P., Klinger, Y., Rice, J.R., 2007. Off-fault damage patterns due to supershear ruptures with application to the 2001 Mw 8.1 Kokoxili (Kunlun) Tibet earthquake. J. Geophys. Res. 112.

Bouchon, M., Karabulut, H., 2008. The aftershock signature of supershear earthquakes. Science 320, 1323–1325.

Bouchon, M., Vallée, M., 2003. Observation of long supershear rupture during the magnitude 8.1 Kunlunshan earthquake. Science 301, 824–826.

Bouchon, M., Toksoz, M.N., Karabulut, H., Bouin, M.-P., Dietrich, M., Aktar, M., Edie, M., 2000. Seismic imaging of the 1999 Izmit (Turkey) rupture inferred from the near-fault recordings. Geophys. Res. Lett. 27 (18), 3013–3016.

Bouchon, M., Bouin, M.-P., Karabulut, H., Toksoz, M.N., Dietrich, M., Rosakis, A.J., 2001. How fast is rupture during an earthquake? New insights from the 1999 Turkey earthquakes. Geophys. Res. Lett. 28, 2723–2726.

Burridge, R., 1973. Admissible speeds for plane-strain shear cracks with friction but lacking cohesion. Geophys. J. R. Astron. Soc. 35, 439–455.

Chester, F.M., Evans, J.P., Biegel, R.L., 1993. Internal structure and weakening mechanisms of the San Andreas Fault. J. Geophys. Res. 98, 771–786.

Das, S., Aki, K., 1977. A numerical study of two-dimensional spontaneous rupture propagation. Geophys. J. R. Astron. Soc. 50, 643–668.

Day, S.M., 1982. Three-dimensional finite difference simulation of fault dynamics: rectangular faults with fixed rupture velocity. Bull. Seismol. Soc. Am. 72, 705–727.

Day, S.M., Dalguer, L.A., Lapusta, N., Liu, Y., 2005. Comparison of finite difference and boundary integral solutions to three-dimensional spontaneous rupture. J. Geophys. Res. 110.

Day, S.M., Gonzalez, S.H., Anooshehpoor, R., Brune, J.N., 2008. Scale-model and numerical simulations of near-fault seismic directivity. Bull. Seismol. Soc. Am. 98, 1186–1206.

Duan, B., Day, S.M., 2008. Inelastic strain distribution and seismic radiation from rupture of a fault. J. Geophys. Res. 113.

Dunham, E.M., 2007. Conditions governing the occurrence of supershear ruptures under slip-weakening friction. J. Geophys. Res. 112.

Dunham, E.M., Archuleta, R.J., 2004. Evidence for a supershear transition during the 2002 Denali fault earthquake. Bull. Seismol. Soc. Am. 94, 256–268.

Dunham, E.M., Archuleta, R.J., 2005. Near-source ground motion from steady state dynamic rupture pulses. Geophys. Res. Lett. 32.

Dunham, E.M., Bhat, H.S., 2008. Attenuation of radiated ground motion and stresses from three-dimensional supershear ruptures. J. Geophys. Res. 113.

Dunham, E.M., Favreau, P., Carlson, J.M., 2003. A supershear transition mechanism for cracks. Science 299, 256–268.

Ellsworth, W.L., Celebi, M., Evans, J.R., Jensen, E.G., Kayen, R., Metz, M.C., Nyman, D.J., Roddick, J.W., Spudich, P., Stephens, C.D., 2004. Near-field ground motion of the 2002 Denali Fault, Alaska, earthquake recorded at Pump Station 10. Earthquake Spectra 20 (3), 597–615.

Festa, G., Vilotte, J.P., 2006. Influence of the rupture initiation on the intersonic transition: crack-like versus pulse-like modes. Geophys. Res. Lett. 33 (15), L15320.

Finzi, Y., Hearn, E.H., Zion, Y.B., Lyakhovsky, V., 2009. Structural properties and deformation patterns of evolving strike-slip faults: numerical simulations incorporating damage rheology. Pure Appl. Geophys. 166, 1537–1573.

Fukuyama, E., Olsen, K.B., 2002. A condition for super-shear rupture propagation in a heterogeneous stress field. Pure Appl. Geophys. 157, 2047–2056.

Haeussler, P.J., Schwartz, D.P., Dawson, T.E., Stenner, H.D., Lienkaemper, J.J., Sherrod, B., Cinti, F.R., Montone, P., Craw, P.A., Crone, A.J., Personius, S.F., 2004. Surface rupture and slip distribution of the Denali and Totschunda faults in the 3 November 2002 M 7.9 earthquake, Alaska. Bull. Seismol. Soc. Am. 94, S23–S52.

Harris, R.A., Barall, M., Archuleta, R., Dunham, E., Aagaard, B., Ampuero, J.-P., Andrews, D.J., Bhat, H., Cruz-Atienza, V., Dalguer, L., Day, S., Duan, B., Ely, G., Kaneko, Y., Kase, Y., Lapusta, N., Liu, Y., Ma, S., Oglesby, D., Olsen, K., Pitarka, A., Song, S., Templeton, E., 2009. The SCEC/USGS dynamic earthquake rupture code validation exercise. Seismol. Res. Lett. 80 (1), 119–126.

Heaton, T.H., 1990. Evidence for and implications of self-healing pulses of slip in earthquake rupture. Phys. Earth Planet. Inter. 64, 1–20.

Hsu, Y.-J., Simons, M., Avouac, J.-P., Galetzka, J., Sieh, K., Chlieh, M., Natawidjaja, D., Prawirodirdjo, L., Bock, Y., 2006. Frictional afterslip following the 2005 Nias-Simeulue Earthquake, Sumatra. Science 312.

Ida, Y., 1972. Cohesive force across the tip of a longitudinal-shear crack and Griffith's specific surface energy. J. Geophys. Res. 77, 3796–3805.

Kaneko, Y., Lapusta, N., Ampuero, J.-P., 2008. Spectral element modeling of spontaneous earthquake rupture on rate and state faults: effect of velocity-strengthening friction at shallow depths. J. Geophys. Res. 113.

Komatitsch, D., Tromp, J., 1999. Introduction to the spectral element method for three-dimensional seismic wave propagation. Geophys. J. Int. 139, 806–822.

Komatitsch, D., Vilotte, J.-P., 1998. The spectral element method: an efficient tool to simulate the seismic response of 2D and 3D geological structures. Bull. Seismol. Soc. Am. 88, 368–392.

Konca, O.A., Leprince, S., Avouac, J.-P., Helmberger, D.V., 2010. Rupture process of the 1999 Mw 7.1 Duzce earthquake from joint analysis of SPOT, GPS, InSAR, strong-motion, and teleseismic data: a supershear rupture with variable rupture velocity. Bull. Seismol. Soc. Am. 100, 267–288.

Lapusta, N., Liu, Y., 2009. Three-dimensional boundary integral modeling of spontaneous earthquake sequences and aseismic slip. J. Geophys. Res.

Liu, Y., Lapusta, N., 2008. Transition of mode II cracks from sub-Rayleigh to intersonic speeds in the presence of favorable heterogeneity. J. Mech. Phys. Solids 56, 25–50.

Lu, X., Lapusta, N., Rosakis, A.J., 2007. Pulse-like and crack-like ruptures in experiments mimicking crustal earthquakes. Proc. Natl Acad. Sci. USA.

Lu, X., Lapusta, N., Rosakis, A.J., 2009. Analysis of supershear transition regimes in rupture experiments: the effect of nucleation conditions and friction parameters. Geophys. J. Int. 177 (2), 717–732.

Ma, S., 2008. A physical model for widespread near-surface and fault zone damage induced by earthquakes. Geochem. Geophys. Geosyst. 9.

Madariaga, R., Olsen, K.B., 2000. Criticality of rupture dynamics in 3-D. Pure Appl. Geophys. 157, 1981–2001.

Marone, C., 1998. Laboratory-derived friction laws and their application to seismic faulting. Annu. Rev. Earth Planet. Sci. 26, 643–696.

Marone, C., Scholz, C.H., Bilham, R., 1991. On the mechanics of earthquake afterslip. J. Geophys. Res. 96 8,441-8,452.

Olsen, K.B., Madariaga, R., Archuleta, R.J., 1997. Three-dimensional dynamic simulation of the 1992 Landers earthquake. Science 278, 834–838.

Olsen, K.B., Minster, J.B., Cui, Y., Chourasia, A., Okaya, D., Maechling, P., Jordan, T., 2008. TeraShake2: spontaneous rupture simulations of Mw 7.7 earthquakes on the southern San Andreas fault. Bull. Seismol. Soc. Am. 98 (3), 1162–1185.

Palmer, A.C., Rice, J.R., 1973. The growth of slip surfaces in the progressive failure of over-consolidated clay. Proc. R. Soc. Lond. A332, 527–548.

Rice, J.R., 1993. Spatio-temporal complexity of slip on a fault. J. Geophys. Res. 98 (B6) 9,885-9,907.

Rice, J.R., Ruina, A.L., 1983. Stability of steady frictional slipping. J. Appl. Mech. 50, 343–349.

Robinson, D.P., Brough, C., Das, S., 2006. The Mw 7.8, 2001 Kunlunshan earthquake: extreme rupture speed variability and effect of fault geometry. J. Geophys. Res. 111.

Rojas, O., Dunham, E., Day, S., Dalguer, L.A., Castillo, J., 2009. Finite difference modeling of rupture propagation with strong velocity-weakening friction. Geophys. J. Int.

Rosakis, A.J., Samudrala, O., Coker, D., 1999. Cracks faster than the shear wave speed. Science 284, 1337–1340.

Ruina, A.L., 1983. Slip instability and state variable friction laws. J. Geophys. Res. 88 (10) 10,359-10,370, 370.

Shearer, P., Hauksson, E., Lin, G., 2005. Southern California hypocenter relocation with waveform cross-correlation, Part 2: Results using source-specific station terms and cluster analysis. Bull. Seismol. Soc. Am. 95 (3), 904–915.

Shi, Z., Ben-Zion, Y., Needleman, Y., 2008. Properties of dynamic rupture and energy partition in a two-dimensional elastic solid with a frictional interface. J. Mech. Phys. Solids 56, 5–24.

Spudich, P., Cranswick, E., 1984. Direct observation of rupture propagation during the 1979 Imperial Valley earthquake using a short baseline accelerometer array. Bull. Seismol. Soc. Am. 74 (6), 2083–2114.

Templeton, E.L., Rice, J.R., 2008. Off-fault plasticity and earthquake rupture dynamics, 1. Dry materials or neglect of fluid pressure changes. J. Geophys. Res. 113.

Vallée, M., Landés, M., Shapiro, N.M., Klinger, Y., 2008. The 14 November 2001 Kokoxili (Tibet) earthquake: high-frequency seismic radiation originating from the transitions between sub-Rayleigh and supershear rupture velocity regimes. J. Geophys. Res. 113.

Walker, K.T., Shearer, P.M., 2009. Illuminating the near-sonic rupture velocities of the intracontinental Kokoxili Mw 7.8 and Denali fault Mw 7.9 strike-slip earthquakes with global P wave back projection imaging. J. Geophys. Res. 114.

Xia, K., Rosakis, A.J., Kanamori, H., 2004. Laboratory earthquakes: the sub-Rayleigh-to-supershear transition. Science 303, 1859–1861.

Yamashita, T., 2000. Generation of microcracks by dynamic shear rupture and its effects on rupture growth and elastic wave radiation. Geophys. J. Int. 143, 395–406.